Supplement of

Complex refractive indices of flame soot from different combustion conditions retrieved using Mie and RDG-FA theories: a simulation chamber study

Johannes Heuser et al.

Figure S1. (Left) Size-dependent effective density ($\rho_{eff}(D_m)$) for the five investigated cast soot (CS1-CS5). Data are acquired between a few minutes and 30 minutes after soot injection in the chamber. The power-law fit $\rho_{eff}(D_m) = a(D_m)^{D_{fm}-3}$(Park et al., 2003) is also plotted with its fitting uncertainty (shaded area). The D_{fm} is the mass-mobility exponent, a parameter describing the morphology of the aerosols. The D_{fm} equals 3 for spherical particles and lies around 2.2 for soot particles (Sorensen, 2011). The D_{fm} is 2.10 for CS1-CS3, increasing to 2.20 and 2.25 for CS4 and CS5. (Right) Transmission electron microscopy images illustrating the morphology of the five CSs as collected 20 to 45 min after injection in CESAM. Adapted from Heuser et al. (2025).

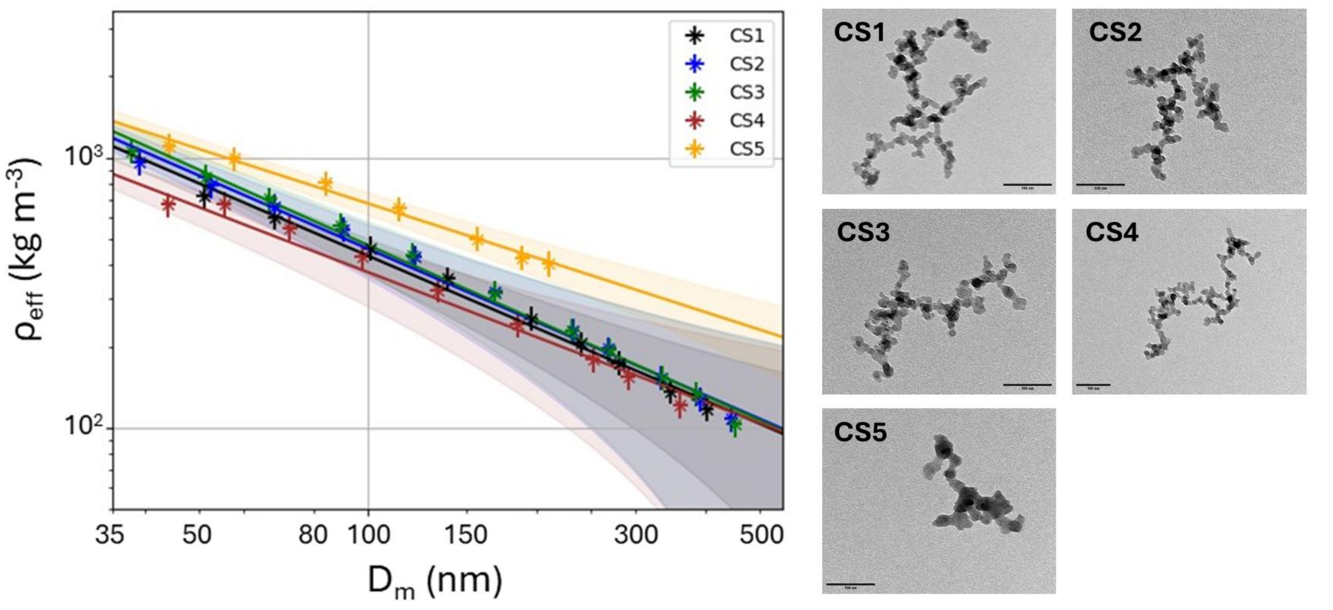

Figure S2. Comparison of calculated and measured b_{scat} and $b_{ext} = b_{scat} + b_{abs}$ (Mie) and b_{scat} and b_{abs} (RDG-FA) at 3-minutes resolution during experiments. Calculated values correspond to (left) Mie calculations using as input the native SMPS number size distribution expressed as mobility diameter (D_m), (centre) Mie calculations using as input the number size distribution expressed as volume-equivalent diameter (D_{ve}), and (right) RDG-FA calculations using as input the number size distribution expressed as gyration diameter (D_g). Displayed values summarise the data from all wavelengths (450, 550, 630 nm) and the five CS1-CS5 soot types. Results of the linear fits between the calculated and measured b_{scat}, b_{ext} and b_{abs}, and correlation coefficients (R^2) are also provided.

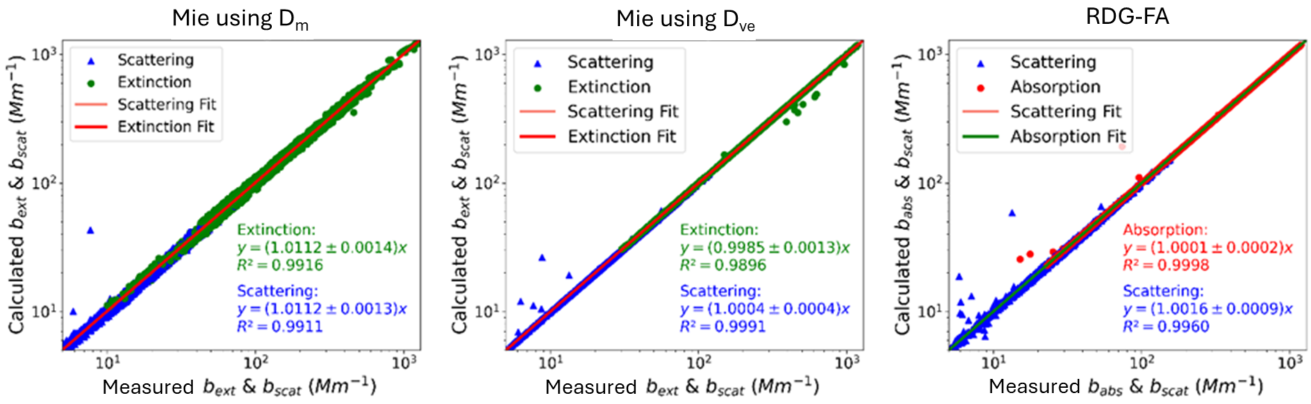

Figure S3. (Top panel) Timeline of the count median diameter expressed as mobility diameter (CMD), and (centre and bottom panels) of the real (n) and imaginary (k) parts of the complex refractive index at 550 nm, calculated via Mie theory with the mobility diameter (Dm) or with the volume-equivalent diameter (Dve), as well as via the RDG-FA approach, for an exemplary CS2 experiment. The values illustrate data evolution over the course of a full experiment, thereby extending beyond the 2 hours after injection considered in the refractive index synthesis.

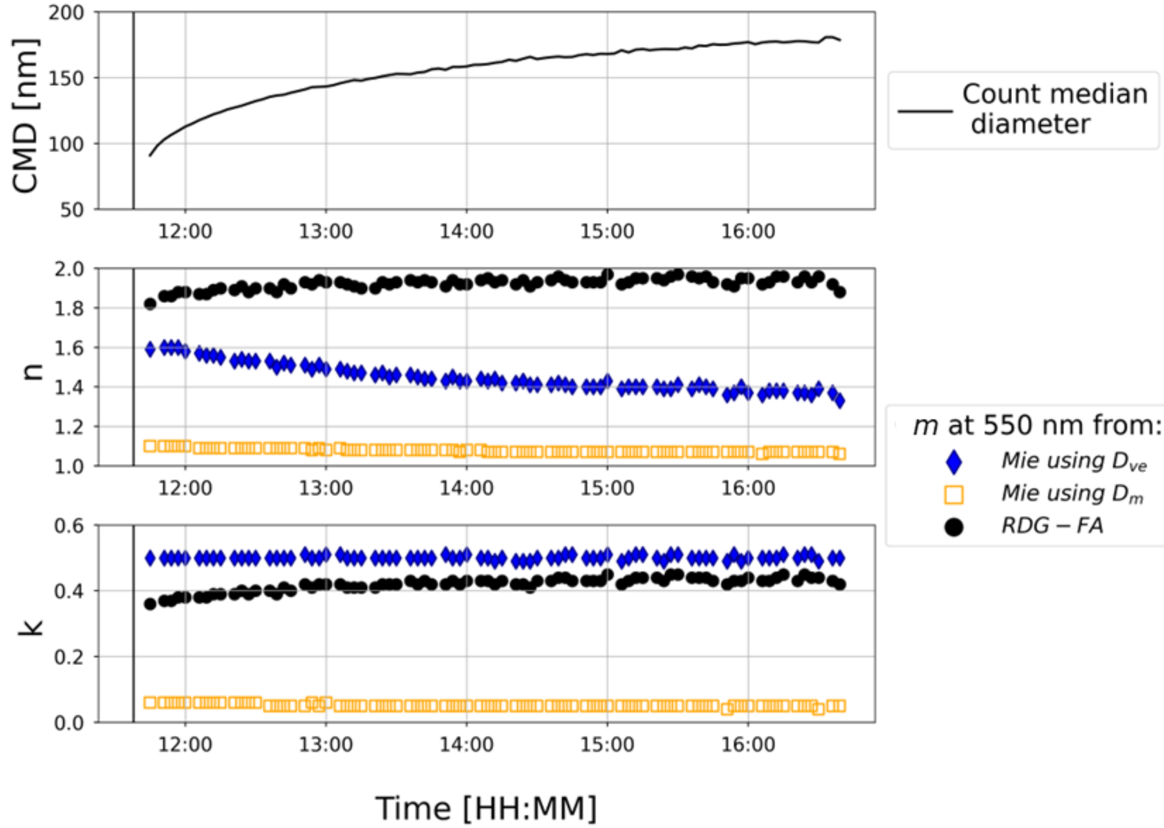

Figure S4. Same as Fig. S3 for CS3.

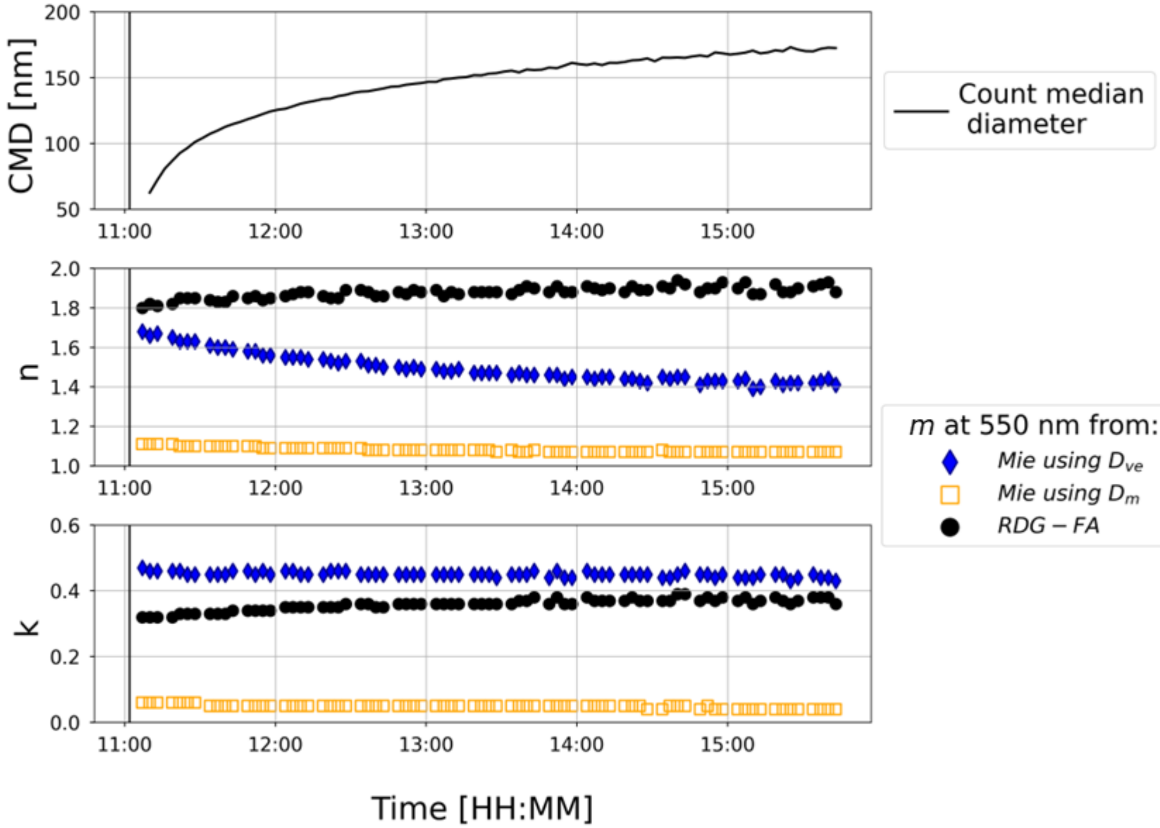

Figure S5. Same as Fig. S3 for CS4.

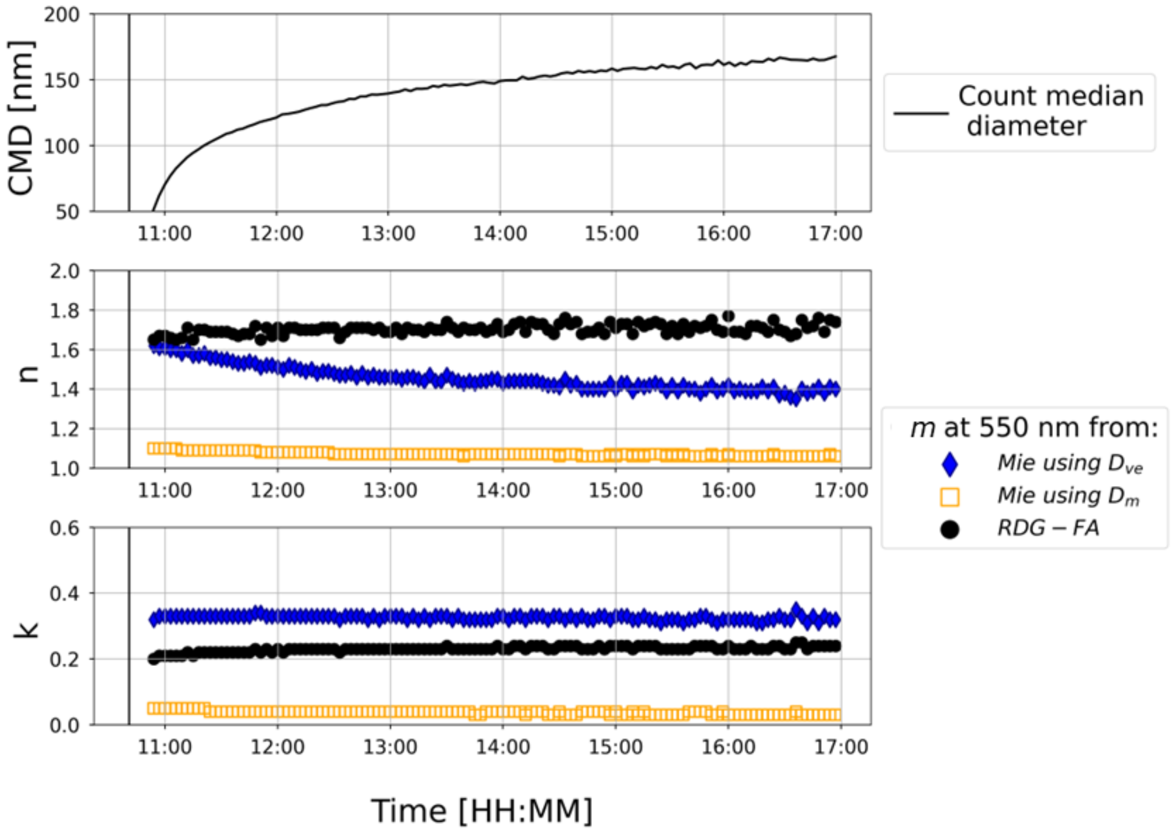

Figure S6. Same as Fig. S3 for CS5.

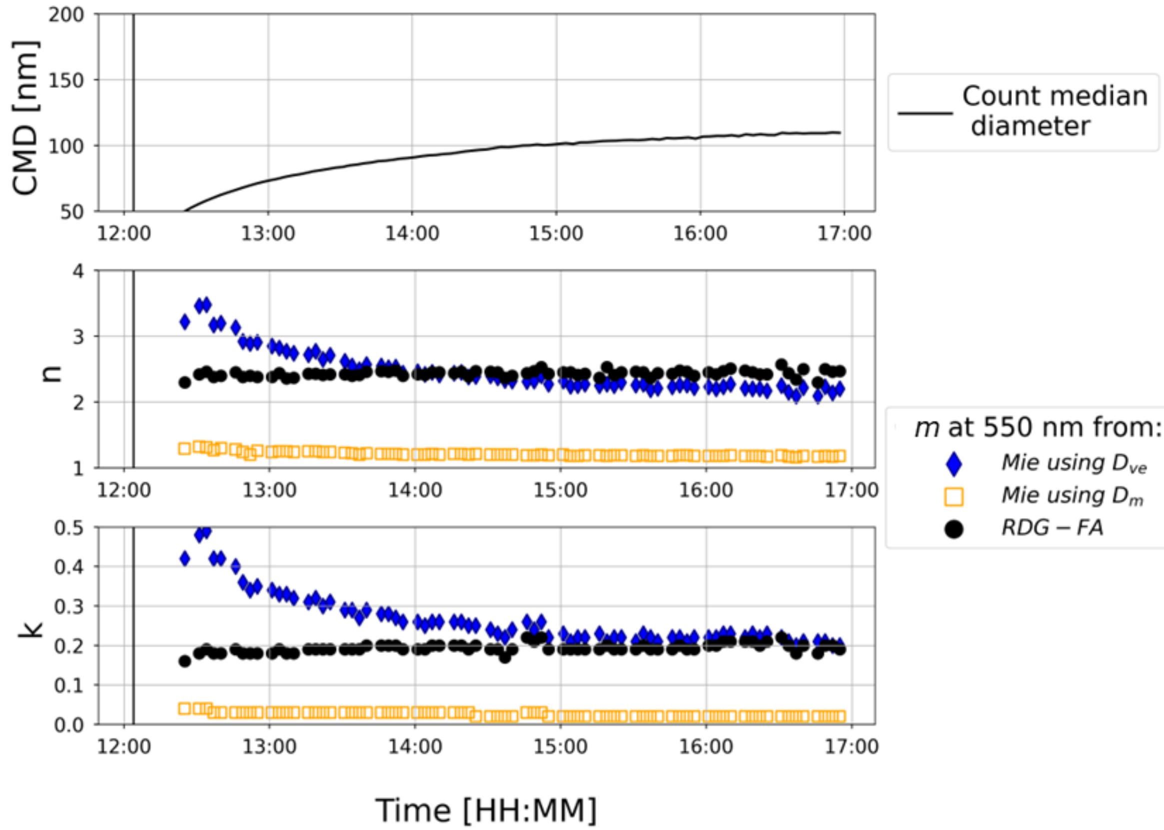

Figure S7. Same as Fig. S3 showing the results at the three wavelengths in this study (450, 550, 630 nm) for CS1 soot.

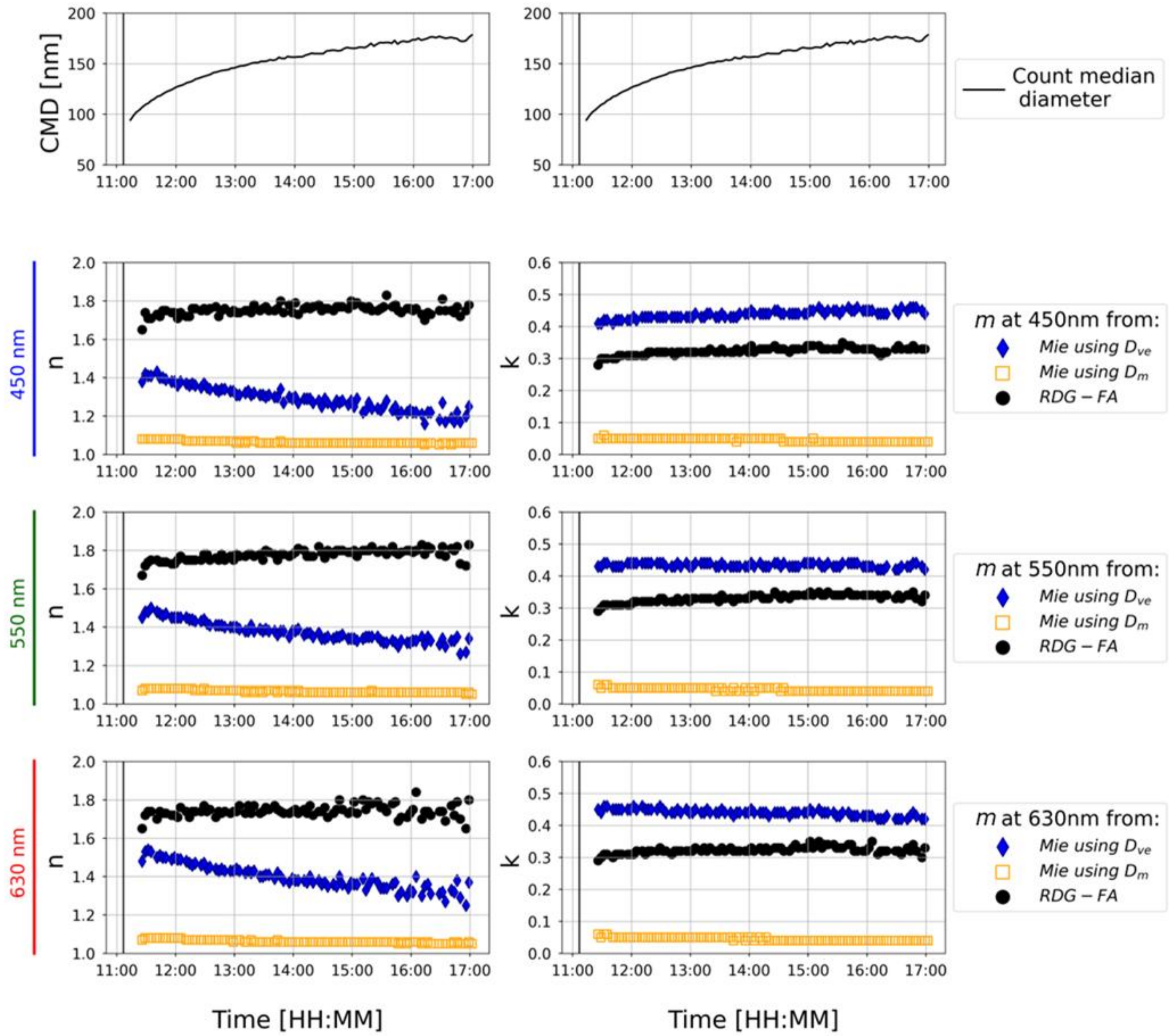

60

Figure S8. Same as Fig. S3 showing the results at the three wavelengths in this study (450, 550, 630 nm) for CS5 soot.

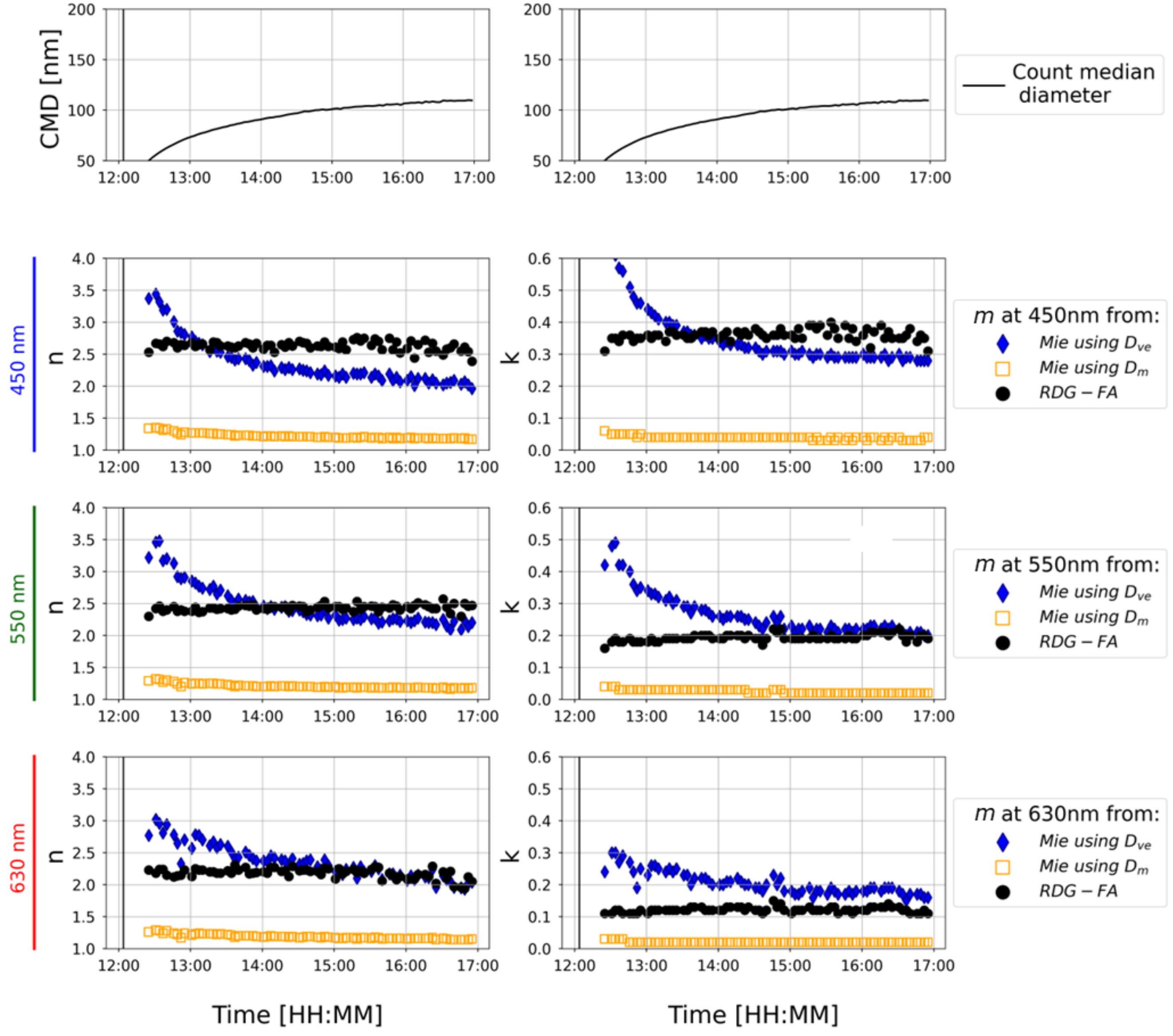

65

Figure S9. Comparison of calculated and measured b_{scat} and $b_{ext} = b_{scat} + b_{abs}$ (Mie) and b_{scat} and b_{abs} (RDG-FA) at 3-minutes resolution during experiments. Calculated values correspond to (left) Mie calculations using as input the SMPS number size distribution expressed as volume-equivalent diameter (D_{ve}), and (right) RDG-FA calculations using as input the number size distribution expressed as gyration diameter (D_g). Displayed values summarise the data from all wavelengths (450, 550, 630 nm) and the five CS1-CS5 soot types. Results of the linear fits between the calculated and measured b_{scat}, b_{ext} and b_{abs}, and correlation coefficients (R^2) are also provided.

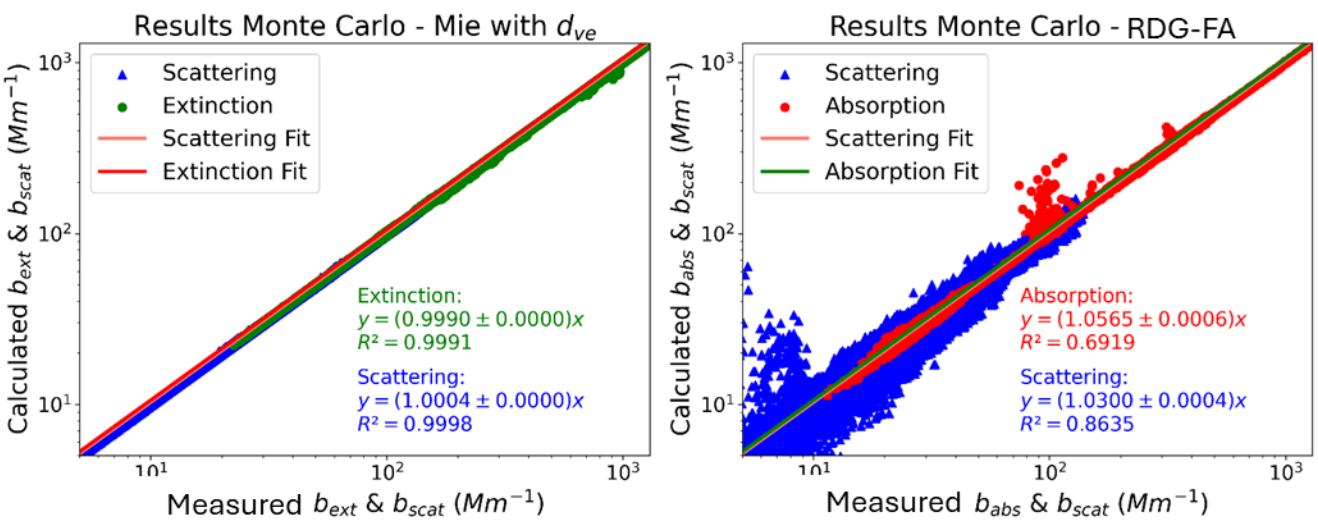

Figure S10. Probability density functions (PDFs) of the real (n) and imaginary (k) parts of the complex refractive index at 450 nm for CS1-CS5 from the Mie based Monte Carlo simulations. The fitting curves of the normal distributions are provided together with vertical lines marking the mode as well as the lower and upper standard deviations.

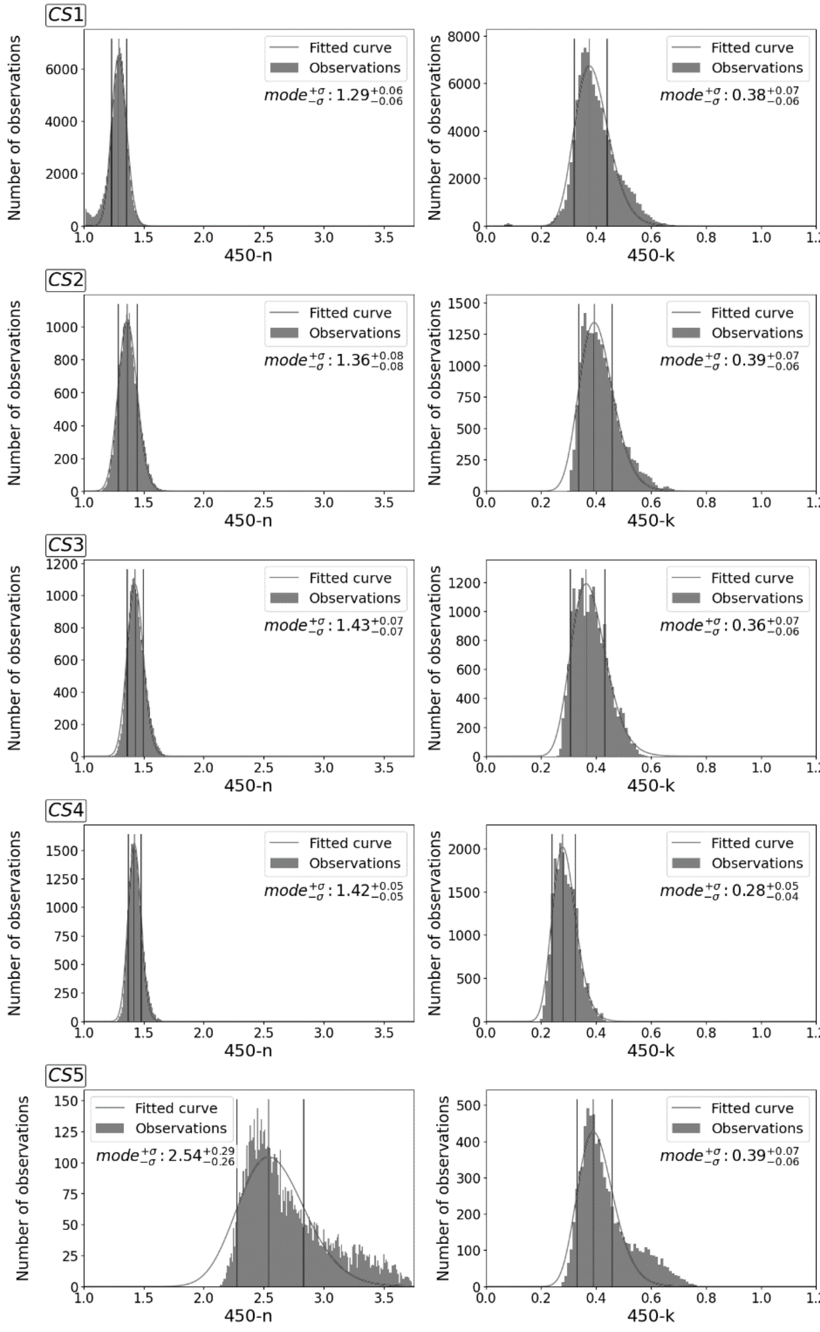

Figure S11. Same as Fig. S10 at 550 nm.

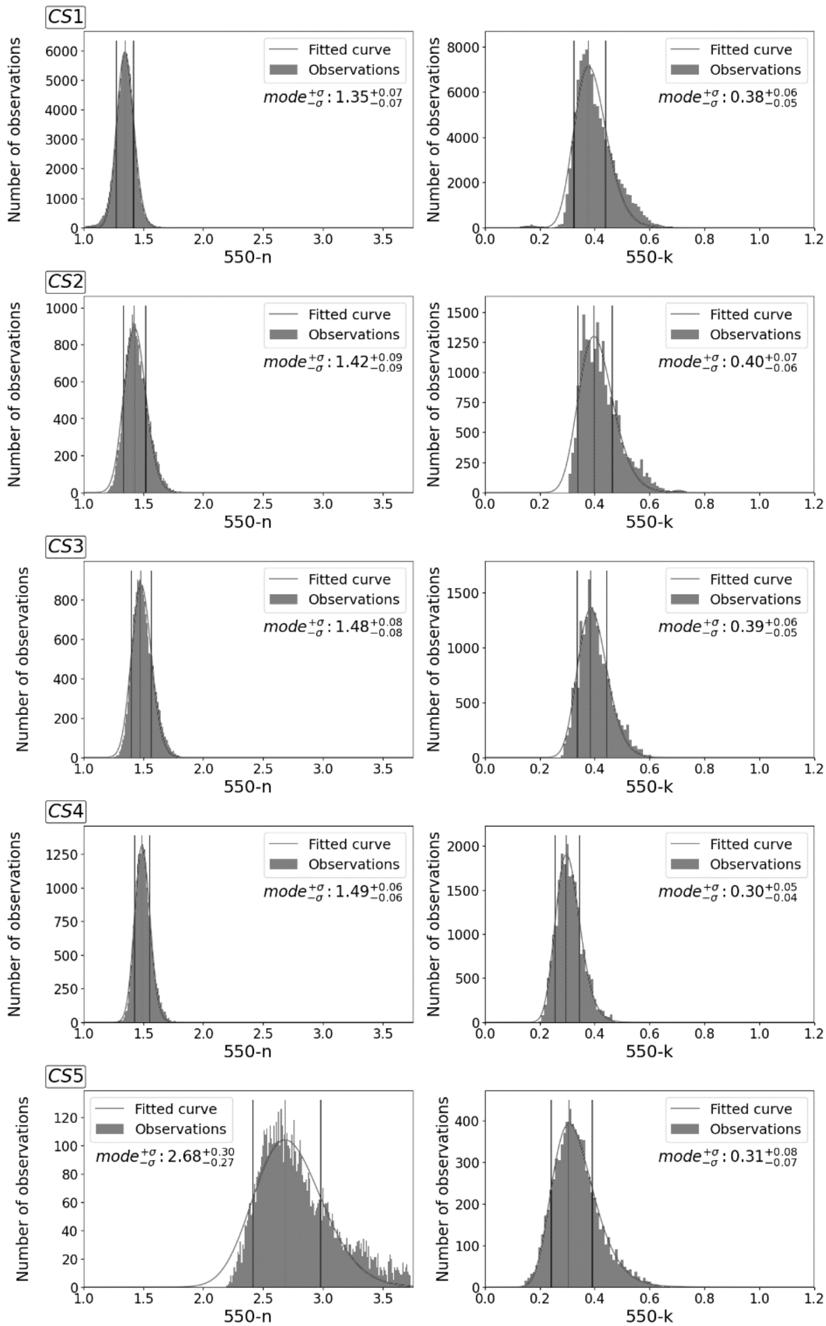

Figure S12. Same as Fig. S10 at 630 nm.

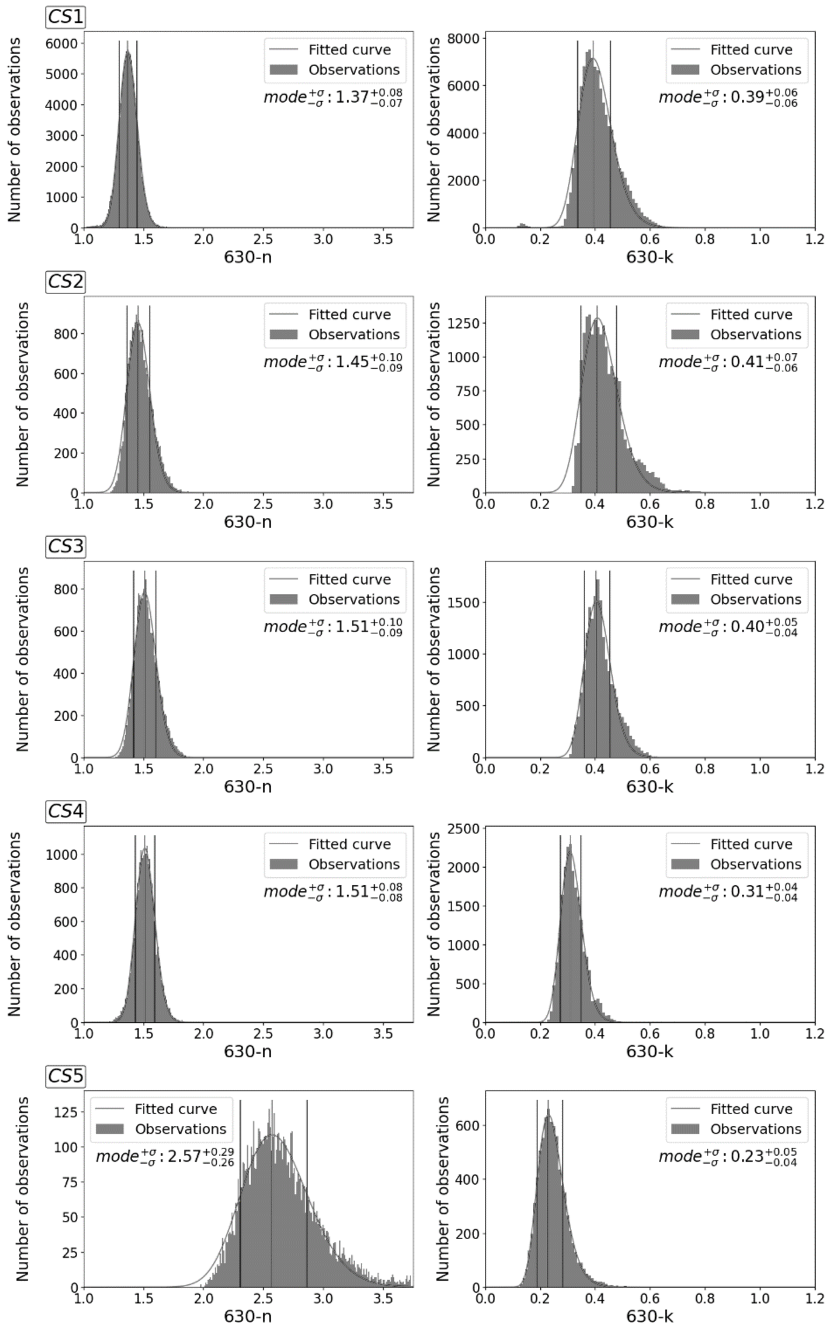

Figure S13. Probability density functions (PDFs) of the real (n) and imaginary (k) parts of the complex refractive index at 450 nm for CS1-CS5 from the RDG-FA based Monte Carlo simulations. The fitting curves of the normal distributions are provided together with vertical lines marking the mode as well as the lower and upper standard deviations.

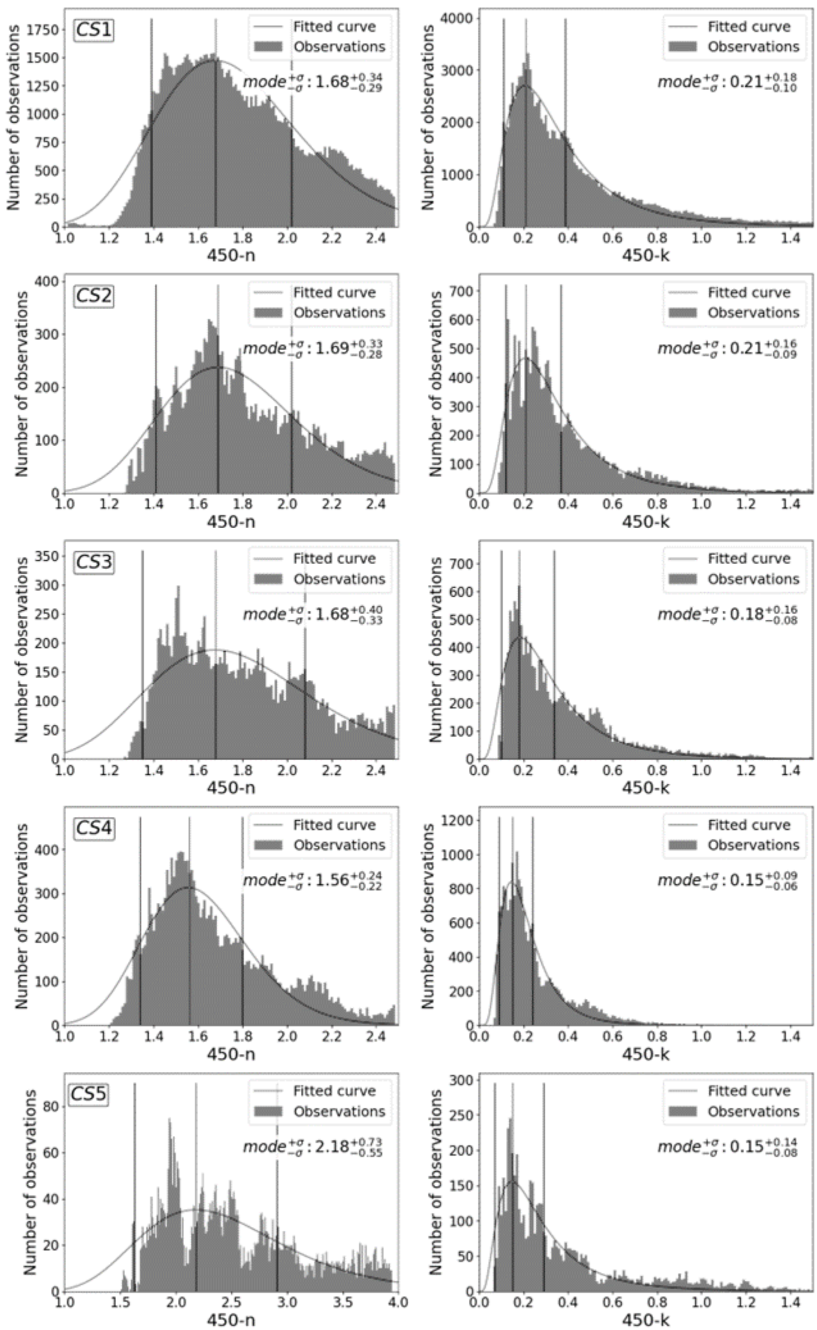

Figure S14. Same as Fig. S13 at 550 nm.

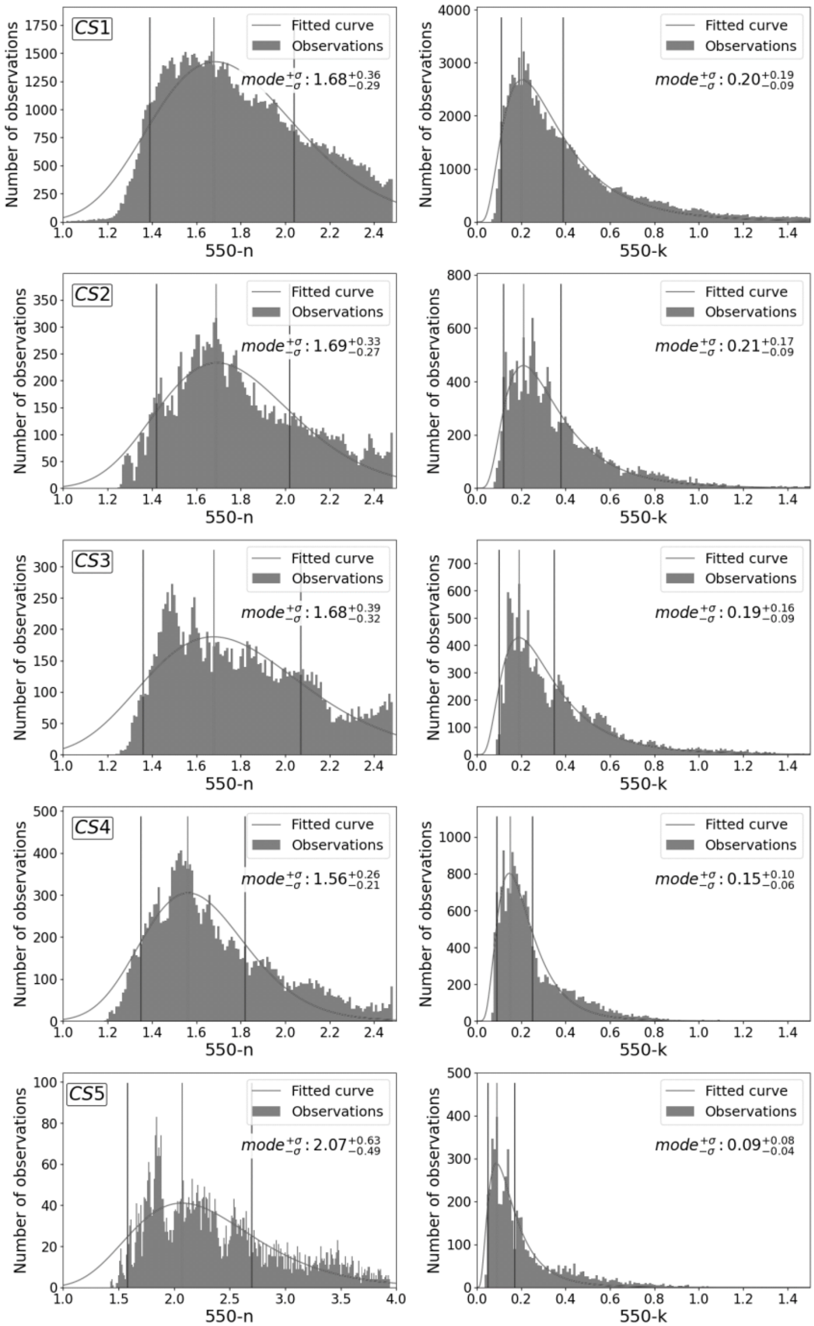

Figure S15. Same as Fig. S13 at 630 nm.

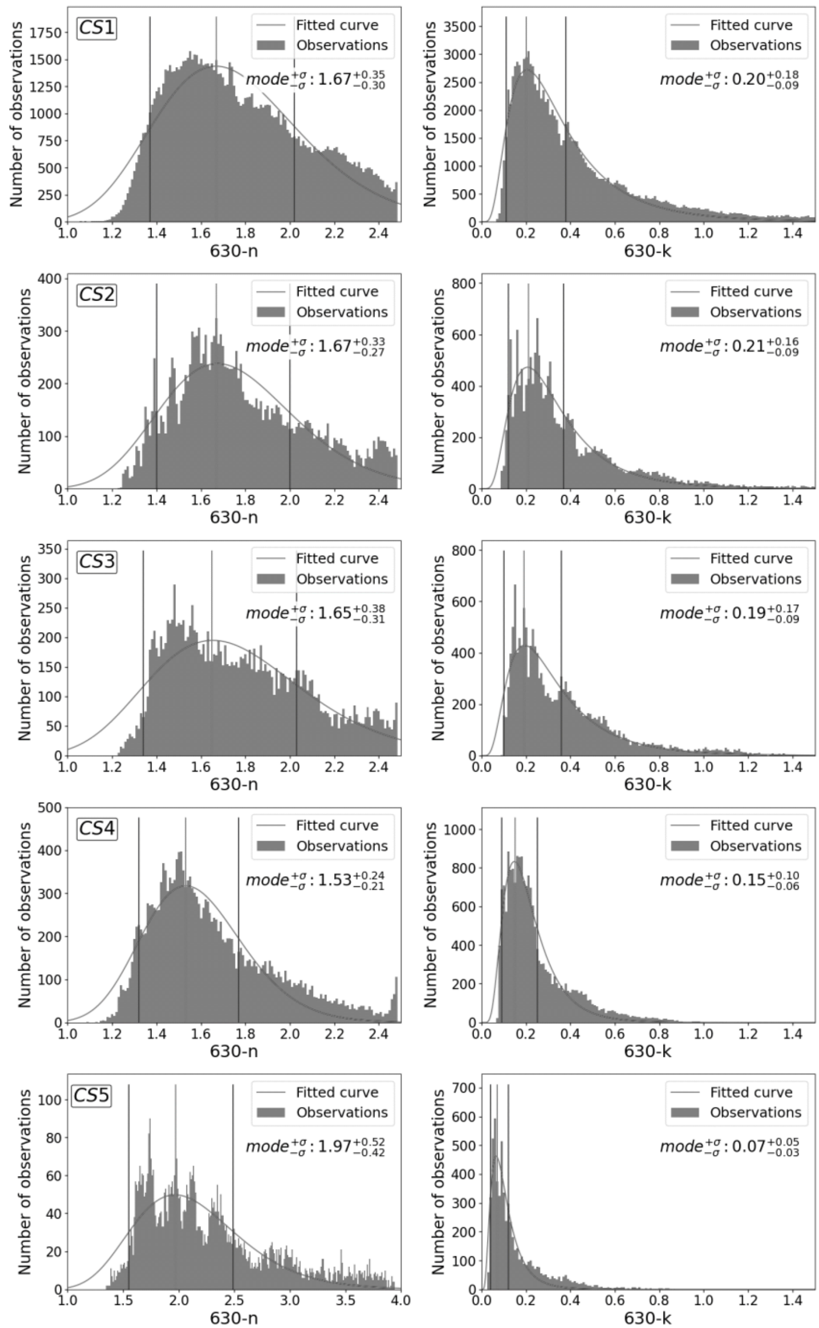

Figure S16. Normalized deviation of the real (n) and imaginary (k) parts of the complex refractive index at 550 nm retrieved using Mie theory from the reference refractive index as a function of the geometric mean diameter (GMD) and geometric standard deviation (σ) of the aerosol size distribution. The difference between Mie and reference values is normalized by the maximum physically plausible range of variation for each component to facilitate comparison of the relative changes in the real and imaginary parts. For the normalization, it is assumed that the real part of the refractive index of the aerosol cannot be smaller than 1, resulting in normalization factors of 0.95 for n (1.95 − 1.00) and 0.79 for k. More details are provided in Supplementary Text S1.

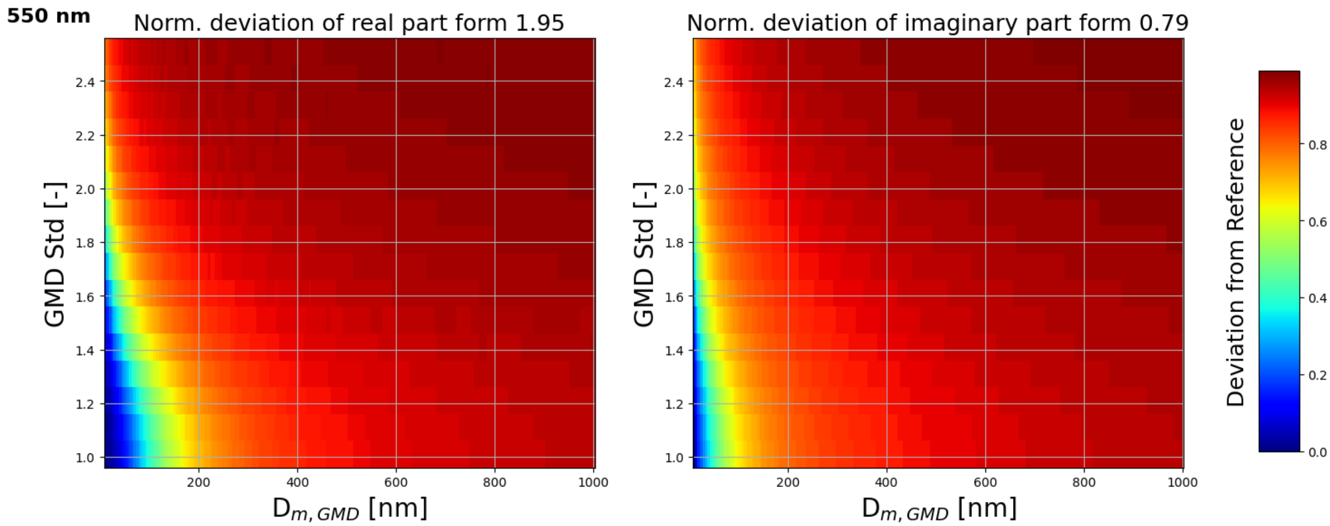

Table S1. List of CESAM soot experiments analysed in the present work. Information includes the experiment name and the investigated conditions, the length of the measurement interval considered for complex refractive index retrieval (dry, dark conditions, no chemical ageing), the total soot lifetime inside the chamber, and the initial soot mass concentration. The list of digital object identifiers (DOI) for the experimental data are also reported. Those data are available through the Database of Atmospheric Simulation Chamber Studies (DASCS) of the EUROCHAMP Data Centre (https://data.eurochamp.org/data-access/chamber-experiments/) also available via the ACTRIS data portal (https://data.actris.eu/).

Experiment (investigated condition)	**Measurement interval for complex refractive index retrieval (hh:mm)**	**Total lifetime (hh:mm)**	**Initial mass concentration [µg m^{-3}]**	**Date**	**Dataset DOI**
CS1 Lifetime 1 (CS1 coagulation dry 1)	21:51	21:51	63 ± 6	23/02/2021	*https://doi.org/10.25326/8KVR-AA70*
CS1 Lifetime 2 (CS1 coagulation dry 2)	25:36	25:36	198 ± 18	24/02/2021	*https://doi.org/10.25326/M24W-V933*
CS1 Lifetime 3 (CS1 coagulation dry 3)	05:56	05:56	61 ± 6	19/10/2021	https://doi.org/10.25326/5144-DY86
CS2 Lifetime 1 (CS2 coagulation dry 1)	03:05	03:05	99 ± 8	11/03/2021	https://doi.org/10.25326/3EGX-K414
CS2 Lifetime 2 (CS2 coagulation dry 2)	05:05	05:05	95 ± 8	20/10/2021	https://doi.org/10.25326/ET9M-7H20
CS3 Lifetime 1 (CS3 coagulation dry 1)	01:51	01:51	58 ± 5	11/03/2021	https://doi.org/10.25326/7HWB-GT84
CS3 Lifetime 2 (CS3 coagulation dry 2)	04:32	04:32	89 ± 8	26/10/2021	https://doi.org/10.25326/0HMW-HM76
CS4 Lifetime 1 (CS4 coagulation dry 1)	02:59	02:59	23 ± 2	12/03/2021	https://doi.org/10.25326/XPP8-2J07
CS4 Lifetime 2 (CS4 coagulation dry 2)	06:25	06:25	44 ± 4	22/10/2021	https://doi.org/10.25326/VPM3-3W86
CS5 Lifetime 1 (CS5 coagulation dry 1)	03:53	03:53	46 ± 4	28/05/2021	https://doi.org/10.25326/BGCT-4J45
CS5 Lifetime 2 (CS5 coagulation dry 2)	05:52	05:52	65 ± 7	21/10/2021	https://doi.org/10.25326/34DX-YJ98
CS1 + hv 1 (CS1 irradiation dry 1)	02:56	05:01	67 ± 6	17/05/2021	https://doi.org/10.25326/2QRB-4E45
CS1 + hv 2 (CS1 irradiation dry 2)	01:34	02:37	58 ± 6	19/05/2021	https://doi.org/10.25326/8HT1-WA13
CS1 + H2O (CS1 coagulation humid)	01:55	07:11	78 ± 8	26/02/2021	https://doi.org/10.25326/WN6E-0272
CS1 + H2O + hv (CS1 irradiation humid)	01:32	06:46	79 ± 8	01/03/2021	https://doi.org/10.25326/EAQE-VX80
CS1 + O3 + hv (CS1 O_3 irradiation humid 1)	01:42	07:48	74 ± 7	02/03/2021	https://doi.org/10.25326/JRAC-4W36
CS1 + SO2 + hv (coating formation, CS1 H_2SO_4-low)	01:32	06:50	90 ± 8	03/03/2021	https://doi.org/10.25326/76FN-TA55
CS1 + O3 + SO2 + hv 1 (coating formation, CS1 H_2SO_4-high1)	01:37	24:48	89 ± 9	04/03/2021	https://doi.org/10.25326/PWHP-ED62

CS1 + O3 + SO2 + hv 2 (coating formation, CS1 H_2SO_4-high2)	02:08	25:16	80 ± 8	09/03/2021	https://doi.org/10.25326/A18P-JF85
CS1 + O3 + AP (coating formation, CS1 SOA-S_{ref})	02:01	24:43	63 ± 6	18/05/2021	https://doi.org/10.25326/AK6B-ZA08
CS1 + O3 + AP high (coating formation, CS1 SOA_{high}-S_{high})	02:12	27:03	169 ± 18	20/05/2021	https://doi.org/10.25326/N7S0-S115
CS1 + O3 + AP low (coating formation, CS1 SOA-S_{low})	02:29	07:22	13 ± 2	26/05/2021	https://doi.org/10.25326/BGRM-3554

Table S2. List of key instrumentation used to determine properties of the aerosol particulate phase during the soot experiments in CESAM. Instrument model, measured or derived parameters, time resolution, uncertainty, and main reference or specific data treatment for each technique are provided. For all optical instruments, measurements on HEPA-filter and on the aerosol-free chamber were used to determine their current instrumental background noise level, then used to determine the noise-signal-ratio and components of the uncertainty.

Instrument	Measured or derived parameter (units)	Time resolution	Associated Uncertainties		Reference
SMPS System TSI SMPS DMA 3080 & CPC 3772	number size distribution [# cm^{-3}] 19.5 to 881.7 nm	180 s	3% + counting error	Error propagation considering 3% DMA uncertainty in particle mobility size selection plus counting error as the standard deviation of an assumed Poisson distribution	(DeCarlo et al., 2004)
TSI DMA 3080 + CPMA (Cambustion) + CPC 3775 high	ρ_{eff} (eff. density) [g cm^{-3}] from the mass-resolved number size distribution [# cm^{-3}]	30-45min with 180 s at each mass	10%	Error propagation considering DMA uncertainty, mass-to-charge uncertainty, relative standard error of the size distribution median diameter For mass calculation, the uncertainty in the power law fit under consideration of the eff. density uncertainties is used	Olfert and Collings (2005) With setup as described by Yon et al. (2015)
TEOM 1400a Thermo Scientific	mass concentration [µg m^{-3}]	300 s	15%	Determined on noise operating on chamber using (determined on clean chamber values and as following smoothed variability)	
CPC 3775 TSI	particle number (> 4 nm) [# cm^{-3}]	1 s	10%	associated uncertainties inside the CESAM system	
SP2 Droplet Measurement Technologies (DMT)	Refractory BC (rBC) mass concentration [µg m^{-3}] rBC number size distribution [# cm^{-3}]	60 s	17%	following the observations by Laborde et al. (2012)	Stephens et al., (2003)
Integrating Nephelometer 3563 TSI	scattering coef. [Mm^{-1}] at 450, 550 & 700 nm	1 s	8%	Propagation of uncertainties from cross-calibration (against freshly calibrated Nephelometer), truncation correction, and signal-to-noise ratio (averaged for different total loss conditions)	Description in Anderson et al. (1996) Trunc. corrected using Massoli et al. (2009)
CAPS PM_{ex} Aerodyne	extinction coef. [Mm^{-1}] 2 inst. = 2 wavelength (450, 630nm)	1 s	5-6%	Propagation of uncertainties for general measurement precision (3%, Massoli et al., 2010) and signal-to-noise ratio (averaged for different total loss conditions)	Kebabian et al. (2007) & Massoli et al. (2010)

CAPS PM_{SSA} Aerodyne	extinction coef. [Mm^{-1}] 2 inst. = 2 wavelength (450, 630nm) (only extinction signal used)	1 s	5-6%	Propagation of uncertainties for general measurement precision and signal-to-noise ratio (see above)	Onasch et al. (2015)
CAPS PM_{ex} Aerodyne / Integrating Nephelometer 3563 TSI	absorption coef. [Mm^{-1}] 2 inst. = 2 wavelength (450, 630nm) (extinction minus scattering)	1 s	10-30%	Propagation of uncertainties from the measurements of scattering and absorption including the uncertainties from the interpolation of the scattering signal to 630 nm	
MAAP Thermo-Scientific	absorption coef. [Mm^{-1}] at 637 nm wavelength	60 s	12%	Provided in instruments literature	Petzold and Schönlinner (2004) & Petzold et al. (2005)
TOF - ACSM Aerodyne Research	non-refractory aerosol composition [$\mu g\ m^{-3}$]	360 s	up to 40% (Strongly varying for experiments)	Uncertainty determined from averaged standard deviations of clean air measurements and the intensity of the signal	
Aethalometer (AE33 – dual spot) Magee Scientific	absorption coefficient [Mm^{-1}] 370, 470, 520, 590, 660, 880, 950 nm	60 s	12%	Propagation of uncertainty in Pattenuation (following Backman et al. (2017) and using clean air measurements), the Cref, and the loading correction	Drinovec et al. (2015)
MWAA (Multi-Wavelength Absorbance Analyser)	Abs. coef. [Mm^{-1}] at 375, 405, 532, 635, 850 nm	15-120 min	mean - 19%	Provided by Massabò and team (var. based on filter loading)	Massabò et al. (2013)
PP_UniMI (Polar photometer)	Abs. coef. [Mm^{-1}] at 405, 448, 532, 635, 780 nm	15-120 min	mean - 14%	Provided by Vecchi and team (var. based on filter loading)	Vecchi et al. (2014)
OCEC Carbon Aerosol Analyzer Sunset Laboratory	elemental carbon organic carbon mass concentration [$\mu g\ cm^{-2}$]	5 sec to 240 min	14%/19%/ 18% average for EC/OC/TC	Uncertainties are determined inside the VBasic-Version OCEC835 analysis software for each thermogram and then propagated	EUSAAR protocol Cavalli et al. (2010)
TEM	morphology	30 sec to 120 min		for D_{pp}, D_f, and k_f as output from Bescond et al. (2014) used average is determined using a single determination of all CS1 pictures	

Table S3. List of instrumentation used to characterise the gas phase during the soot experiments in CESAM. Instrument model, measured parameters, time resolution, accuracy, and detection limit are given.

Instrument	Parameter (units)	Acquisition resolution (averaged to 1 min)	Accuracy (at 1 min time resolution) & detection limit (Acc./DL)
NO_x Monitor – Horiba APNA370	NO, NO_2 (NOx) [ppb]	5 s	1 / 0.5 ppb
APEE - ProCeas	CO/CO_2 [ppm]	45 s	0.1/ 0.05 ppm
SO_2 Monitor - Horiba APSA370	SO_2 [ppb]	5 s	1/ 0.05 ppb
Ozone (O_3) Monitor - Horiba APOA370	O_3 [ppb]	5 s	1 / 0.05 ppb
Teledyne T500U	NO_2 [ppb]	30 s	0.5% (above 5 ppb)/ 0.04 ppb
Hygrometer - Vaisala HMP234	RH [%] & T [°C]	1 s	2% & ± 0.1 °C (only Acc.)
Baratron type MKS 626AX13TDE (high)/ 626AX11TDE (low)	Pressure [mBar]	1 s	0.25% for 1 to 1000 Torr (Unc.)
PTR-ToF-MS (Kore ltd.)	Mass-loading gaseous components [ppb]	60 s	0.1 ppb [DL]

Table S4. Real (n) and imaginary (k) parts of the complex refractive index retrieved at 450, 550, and 630 nm for CS1-CS5 from Mie D_{ve} and RDG-FA calculations. The mean and standard deviation of the 3-min refractive index data for all the different experiments are reported in the upper part of the table. The Monte Carlo simulation data expressed as the fitting parameters of the calculated probability density functions are reported in the bottom part. The number of experimental data is 382 (CS1), 82 (CS2), 62 (CS3), 44 (CS4), and 27 (CS5).

	Experiment-averaged complex refractive index											
	Mie D_{ve}						**RDG-FA**					
Soot type	**450 nm**		**550 nm**		**630 nm**		**450 nm**		**550 nm**		**630 nm**	
	n ± σ	**k ± σ**	**n ± σ**	**k ± σ**	**n ± σ**	**k ± σ**	**n ± σ**	**k ± σ**	**n ± σ**	**k ± σ**	**n ± σ**	**k ± σ**
CS1	1.27 ± 0.11	0.43 ± 0.09	1.34 ± 0.08	0.43 ± 0.08	1.38 ± 0.08	0.43 ± 0.08	1.71 ± 0.10	0.31 ± 0.07	1.72 ± 0.10	0.31 ± 0.06	1.70 ± 0.10	0.31 ± 0.06
CS2	1.36 ± 0.08	0.42 ± 0.05	1.43 ± 0.08	0.43 ± 0.05	1.46 ± 0.09	0.44 ± 0.06	1.81 ± 0.06	0.31 ± 0.07	1.81 ± 0.07	0.34 ± 0.05	1.78 ± 0.07	0.34 ± 0.04
CS3	1.45 ± 0.06	0.39 ± 0.06	1.52 ± 0.07	0.41 ± 0.04	1.54 ± 0.08	0.43 ± 0.04	1.78 ± 0.09	0.28 ± 0.08	1.77 ± 0.10	0.29 ± 0.05	1.73 ± 0.09	0.30 ± 0.03
CS4	1.44 ± 0.04	0.29 ± 0.03	1.51 ± 0.04	0.31 ± 0.02	1.53 ± 0.05	0.33 ± 0.01	1.69 ± 0.06	0.21 ± 0.04	1.67 ± 0.04	0.21 ± 0.03	1.64 ± 0.04	0.21 ± 0.01
CS5	2.72 ± 0.34	0.44 ± 0.09	2.81 ± 0.30	0.34 ± 0.07	2.63 ± 0.19	0.24 ± 0.03	2.64 ± 0.04	0.35 ± 0.01	2.41 ± 0.04	0.19 ± 0.01	2.20 ± 0.04	0.12 ± 0.01
	Monte Carlo simulations											
	Mie D_{ve}						**RDG-FA**					
	450 nm		**550 nm**		**630 nm**		**450 nm**		**550 nm**		**630 nm**	
	n (+σ; -σ)	**k (+σ; -σ)**	**n (+σ; -σ)**	**k (+σ; -σ)**	**n (+σ; -σ)**	**k (+σ; -σ)**	**n (+σ; -σ)**	**k (+σ; -σ)**	**n (+σ; -σ)**	**k (+σ; -σ)**	**n (+σ; -σ)**	**k (+σ; -σ)**
CS1	1.29 (0.06; 0.06)	0.38 (0.07; 0.06)	1.35 (0.07; 0.07)	0.38 (0.06; 0.05)	1.37 (0.08; 0.07)	0.39 (0.06; 0.06)	1.68 (0.34; 0.29)	0.21 (0.18; 0.10)	1.68 (0.36; 0.29)	0.20 (0.19; 0.09)	1.67 (0.35; 0.30)	0.20 (0.18; 0.09)
CS2	1.36 (0.08; 0.08)	0.39 (0.07; 0.06)	1.42 (0.09; 0.09)	0.40 (0.07; 0.06)	1.45 (0.10; 0.09)	0.41 (0.07; 0.06)	1.69 (0.33; 0.28)	0.21 (0.16; 0.09)	1.69 (0.33; 0.27)	0.21 (0.17; 0.09)	1.67 (0.33; 0.27)	0.21 (0.16; 0.09)
CS3	1.43 (0.07; 0.07)	0.36 (0.07; 0.06)	1.48 (0.08; 0.08)	0.39 (0.06; 0.05)	1.51 (0.10; 0.09)	0.40 (0.05; 0.04)	1.68 (0.40; 0.33)	0.18 (0.16; 0.08)	1.68 (0.39; 0.32)	0.19 (0.16; 0.09)	1.65 (0.38; 0.31)	0.19 (0.17; 0.09)
CS4	1.42 (0.05; 0.05)	0.28 (0.05; 0.04)	1.49 (0.06; 0.06)	0.30 (0.05; 0.04)	1.51 (0.07; 0.07)	0.31 (0.04; 0.04)	1.56 (0.24; 0.22)	0.15 (0.09; 0.06)	1.56 (0.26; 0.21)	0.15 (0.10; 0.06)	1.53 (0.24; 0.21)	0.15 (0.10; 0.06)
CS5	2.54 (0.29; 0.26)	0.39 (0.07; 0.06)	2.68 (0.30; 0.27)	0.31 (0.08; 0.07)	2.57 (0.29; 0.26)	0.23 (0.05; 0.04)	2.18 (0.74; 0.55)	0.15 (0.14; 0.08)	2.07 (0.65; 0.49)	0.09 (0.08; 0.04)	1.97 (0.53; 0.42)	0.07 (0.05; 0.03)

Table S5. Real (n) and imaginary (k) parts of the complex refractive index retrieved at 450, 550, and 630 nm for CS1-CS5 from Mie D_m calculations. The mean and standard deviation of the 3-min refractive index data for all the different experiments are reported. The number of experimental data is 382 (CS1), 82 (CS2), 62 (CS3), 44 (CS4), and 27 (CS5).

	Experiment-averaged complex refractive index					
	Mie D_m					
Soot type	**450 nm**		**550 nm**		**630 nm**	
	n ± σ	**k ± σ**	**n ± σ**	**k ± σ**	**n ± σ**	**k ± σ**
CS1	1.06 ± 0.01	0.04 ± 0.01	1.06 ± 0.01	0.04 ± 0.01	1.06 ± 0.01	0.04 ± 0.01
CS2	1.07 ± 0.01	0.05 ± 0.01	1.07 ± 0.01	0.05 ± 0.01	1.07 ± 0.01	0.05 ± 0.01
CS3	1.08 ± 0.01	0.05 ± 0.01	1.08 ± 0.01	0.05 ± 0.01	1.08 ± 0.01	0.05 ± 0.01
CS4	1.07 ± 0.01	0.04 ± 0.01	1.07 ± 0.01	0.04 ± 0.01	1.07 ± 0.01	0.04 ± 0.01
CS5	1.22 ± 0.04	0.04 ± 0.01	1.21 ± 0.04	0.03 ± 0.01	1.19 ± 0.04	0.02 ± 0.01

Table S6. Fitting parameters of the real (n) and imaginary (k) parts of the complex refractive index and E(m) at 550 nm for Mie and RDG-FA data, as shown in Fig. 5 in the main manuscript. The correlation coefficient (R^2) is also reported. The asterisk indicates that the fit only considers CS1-CS4 data, instead of CS1-CS5 as for all the other datasets.

Parameter (theory)	**Fitting equation y=ax+b**	**R^2**
n (Mie)	-0.0061x+1.87*	0.67*
k (Mie)	0.0012x+0.32	0.46
E(m) (Mie)	0.0023x+0.051	0.97
n (RDG-FA)	0.0031x+1.53* -0.0086x+2.35	0.32* 0.83
k (RDG-FA)	0.0017x+0.17	0.71
E(m) (RDG-FA)	0.0011x+0.042	0.97

Text S1. Investigating and visualizing the impact of aggregation during time on the complex refractive index retrieved from Mie theory

The results presented in Section 3.2 show a systematic decrease in the real part of the complex refractive index retrieved using Mie theory over time. This trend reflects the limitations of Mie theory in representing changes in the microphysical properties of soot particles.

To further investigate this behaviour, a series of calculations was performed to visualize how the properties of an aerosol size distribution influence the effective refractive index retrieved with Mie theory. First, optical coefficients (b_{scat}, b_{abs}, and b_{ext}) were generated using the RDG-FA, taken as reference theory, and a fixed complex refractive index for a large set of theoretical aerosol size distributions. The size distributions were represented by lognormal distributions whose geometric mean diameter (GMD) and geometric standard deviation (GMD std) were systematically varied, thereby spanning a wide range of particle sizes and degrees of polydispersity. The minimum particle size was limited by the primary particle diameter, which is approximately 10 nm for the soot investigated here. All remaining fractal parameters required for the RDG-FA calculations were taken from the properties of CS1 (see Table 1 in the main manuscript). The reference complex refractive index was selected from the literature. The value reported by Bond and Bergstrom (2006) for black carbon, 1.95-0.79i, was used throughout the calculations.

In a second step, the calculated optical coefficients together with the corresponding theoretical size distributions were used to retrieve an effective complex refractive index using Mie theory. The retrieval was performed with a grid resolution of 0.01 for both the real (n) and imaginary (k) parts of the refractive index. Prior to the retrieval, the theoretical mobility size distributions were converted into volume-equivalent size distributions, as described in the main text, using the properties of CS1. The resulting retrievals provide effective values of n and k for a broad range of aerosol size distributions.

Figure S16 shows the normalized deviation of the retrieved real and imaginary parts of the refractive index from the reference value used in the RDG-FA calculations at a wavelength of 550 nm, as a function of the GMD and GMD std of the size distribution. The results demonstrate that the best agreement between the reference and retrieved refractive indices is obtained when the particles are close in size to the primary particles. As either the geometric standard deviation or the geometric mean diameter increases, the discrepancy between the reference and retrieved values also increases. Both parameters effectively increase the fraction of larger particles within the aerosol population. For soot, larger particles also correspond to increasingly complex aggregate structures. As primary particles assemble into fractal aggregates, the particles deviate progressively from the idealized compact sphere, exhibiting increasing void fractions and more irregular morphologies. Consequently, the observed changes in the retrieved refractive index can be interpreted as compensation by the Mie inversion for its inability to accurately represent the optical properties of non-spherical fractal aggregates. Because this effect is primarily governed by deviations from spherical geometry rather than particle size alone, the magnitude of the discrepancy between the retrieved Mie refractive index and the reference value depends on the specific soot characteristics, including the primary particle size as well as the aggregate morphology, particularly its fractal dimension.

Text S2. Calculations of the radiative forcing

The calculated and measured single scattering albedo (SSA) values in Sect. 5 of the main manuscript were used to determine the change in radiative forcing (RF) by utilizing the simplified formulation by (Haywood and Shine, 1995), providing the instantaneous RF for a thin layer of absorbing aerosols at the top-of-atmosphere. The formulation express RF as:

$$RF = -DS_0 {T_{at}}^2 (1 - A_c)\, SSA\beta\delta \left\{ (1 - R_s)^2 - \left(\frac{2R_s}{\beta}\right) \left[\left(\frac{1}{SSA}\right) - 1 \right] \right\} \qquad (S1)$$

where D is the fractional day length, S_0 the solar constant, T_{at} the atmospheric transmission, A_c the fractional cloud amount, SSA the aerosol single scattering albedo, β the aerosol upscatter fraction of scattering, δ the aerosol optical depth, and R_s the surface reflectivity. Despite Eq. (S1) provides a simplistic estimate of RF considering only aerosol-radiation interactions and not accounting for changes compared to pre-industrial conditions, it can be used to quantify the impact of SSA mispredictions on the soot radiative effect. The relative change of RF due to a change from SSA_{meas} to $SSA_{modelled}$ was determined as:

$$\Delta RF = \frac{RF_{SSA_{modelled}}}{RF_{SSA_{measured}}} = \frac{SSA_{modelled} \left\{ (1 - R_s)^2 - \left(\frac{2R_s}{\beta}\right) \left[\left(\frac{1}{SSA_{modelled}}\right) - 1 \right] \right\}}{SSA_{measured} \left\{ (1 - R_s)^2 - \left(\frac{2R_s}{\beta}\right) \left[\left(\frac{1}{SSA_{measured}}\right) - 1 \right] \right\}} \qquad (S2)$$

For Eq. (S2) the value of R_S was set at 0.2, corresponding to a bare soil. The upscatter fraction β was calculated from a backscattering ratio of 0.27, determined from experimental data using the equations in Moosmüller and Ogren (2017).

References

Anderson, T. L., Covert, D. S., Marshall, S. F., Laucks, M. L., Charlson, R. J., Waggoner, A. P., Ogren, J. A., Caldow, R., Holm, R. L., Quant, F. R., Sem, G. J., Wiedensohler, A., Ahlquist, N. A., and Bates, T. S.: Performance Characteristics of a High-Sensitivity, Three-Wavelength, Total Scatter/Backscatter Nephelometer, J. Atmos. Oceanic Technol., 13, 967–986, https://doi.org/10.1175/1520-0426(1996)013%3C0967:PCOAHS%3E2.0.CO;2, 1996.

Backman, J., Schmeisser, L., Virkkula, A., Ogren, J. A., Asmi, E., Starkweather, S., Sharma, S., Eleftheriadis, K., Uttal, T., Jefferson, A., Bergin, M., Makshtas, A., Tunved, P., and Fiebig, M.: On Aethalometer measurement uncertainties and an instrument correction factor for the Arctic, Atmos. Meas. Tech., 10, 5039–5062, https://doi.org/10.5194/amt-10-5039-2017, 2017.

Bescond, A., Yon, J., Ouf, F. X., Ferry, D., Delhaye, D., Gaffié, D., Coppalle, A., and Rozé, C.: Automated Determination of Aggregate Primary Particle Size Distribution by TEM Image Analysis: Application to Soot, Aerosol Science and Technology, 48, 831–841, https://doi.org/10.1080/02786826.2014.932896, 2014.

Bond, T. C. and Bergstrom, R. W.: Light Absorption by Carbonaceous Particles: An Investigative Review, Aerosol Science and Technology, 40, 27–67, https://doi.org/10.1080/02786820500421521, 2006.

Cavalli, F., Viana, M., Yttri, K. E., Genberg, J., and Putaud, J.-P.: Toward a standardised thermal-optical protocol for measuring atmospheric organic and elemental carbon: the EUSAAR protocol, Atmos. Meas. Tech., 3, 79–89, https://doi.org/10.5194/amt-3-79-2010, 2010.

DeCarlo, P. F., Slowik, J. G., Worsnop, D. R., Davidovits, P., and Jimenez, J. L.: Particle Morphology and Density Characterization by Combined Mobility and Aerodynamic Diameter Measurements. Part 1: Theory, Aerosol Science and Technology, 38, 1185–1205, https://doi.org/10.1080/027868290903907, 2004.

Drinovec, L., Močnik, G., Zotter, P., Prévôt, A. S. H., Ruckstuhl, C., Coz, E., Rupakheti, M., Sciare, J., Müller, T., Wiedensohler, A., and Hansen, A. D. A.: The “dual-spot” Aethalometer: an improved measurement of aerosol black carbon with real-time loading compensation, Atmos. Meas. Tech., 8, 1965–1979, https://doi.org/10.5194/amt-8-1965-2015, 2015.

Haywood, J. M. and Shine, K. P.: The effect of anthropogenic sulfate and soot aerosol on the clear sky planetary radiation budget, Geophysical Research Letters, 22, 603–606, https://doi.org/10.1029/95GL00075, 1995.

Heuser, J., Di Biagio, C., Yon, J., Cazaunau, M., Bergé, A., Pangui, E., Zanatta, M., Renzi, L., Marinoni, A., Inomata, S., Yu, C., Bernardoni, V., Chevaillier, S., Ferry, D., Laj, P., Maillé, M., Massabò, D., Mazzei, F., Noyalet, G., Tanimoto, H., Temime-Roussel, B., Vecchi, R., Vernocchi, V., Formenti, P., Picquet-Varrault, B., and Doussin, J.-F.: Spectral optical properties of soot: laboratory investigation of propane flame particles and their link to composition, Atmospheric Chemistry and Physics, 25, 6407–6428, https://doi.org/10.5194/acp-25-6407-2025, 2025.

Heuser, J., Di Biagio, C., Yon, J., Cazaunau, M., Bergé, A., Pangui, E., Zanatta, M., Renzi, L., Marinoni, A., Yu, C., Chevaillier, S., Ferry, D., Laj, P., Maillé, M., Formenti, P., Picquet-Varrault, B., and Doussin, J.-F.: The synergy of morphology and mixing state on the absorption of coated black carbon soot, EGUsphere, 1–25, https://doi.org/10.5194/egusphere-2026-1867, 2026.

Kebabian, P. L., Robinson, W. A., and Freedman, A.: Optical extinction monitor using cw cavity enhanced detection, Review of Scientific Instruments, 78, 063102, https://doi.org/10.1063/1.2744223, 2007.

Laborde, M., Schnaiter, M., Linke, C., Saathoff, H., Naumann, K.-H., Möhler, O., Berlenz, S., Wagner, U., Taylor, J. W., Liu, D., Flynn, M., Allan, J. D., Coe, H., Heimerl, K., Dahlkötter, F., Weinzierl, B., Wollny, A. G., Zanatta, M., Cozic, J., Laj, P., Hitzenberger, R., Schwarz, J. P., and Gysel, M.: Single Particle Soot Photometer intercomparison at the AIDA chamber, Atmos. Meas. Tech., 5, 3077–3097, https://doi.org/10.5194/amt-5-3077-2012, 2012.

Massabò, D., Bernardoni, V., Bove, M. C., Brunengo, A., Cuccia, E., Piazzalunga, A., Prati, P., Valli, G., and Vecchi, R.: A multi-wavelength optical set-up for the characterization of carbonaceous particulate matter, Journal of Aerosol Science, 60, 34–46, https://doi.org/10.1016/j.jaerosci.2013.02.006, 2013.

Massoli, P., Murphy, D. M., Lack, D. A., Baynard, T., Brock, C. A., and Lovejoy, E. R.: Uncertainty in Light Scattering Measurements by TSI Nephelometer: Results from Laboratory Studies and Implications for Ambient Measurements, Aerosol Science and Technology, 43, 1064–1074, https://doi.org/10.1080/02786820903156542, 2009.

Massoli, P., Kebabian, P. L., Onasch, T. B., Hills, F. B., and Freedman, A.: Aerosol Light Extinction Measurements by Cavity Attenuated Phase Shift (CAPS) Spectroscopy: Laboratory Validation and Field Deployment of a Compact Aerosol Particle Extinction Monitor, Aerosol Science and Technology, 44, 428–435, https://doi.org/10.1080/02786821003716599, 2010.

Moosmüller, H. and Ogren, J. A.: Parameterization of the Aerosol Upscatter Fraction as Function of the Backscatter Fraction and Their Relationships to the Asymmetry Parameter for Radiative Transfer Calculations, Atmosphere, 8, 133, https://doi.org/10.3390/atmos8080133, 2017.

Olfert, J. S. and Collings, N.: New method for particle mass classification—the Couette centrifugal particle mass analyzer, Journal of Aerosol Science, 36, 1338–1352, https://doi.org/10.1016/j.jaerosci.2005.03.006, 2005.

Onasch, T. B., Massoli, P., Kebabian, P. L., Hills, F. B., Bacon, F. W., and Freedman, A.: Single Scattering Albedo Monitor for Airborne Particulates, Aerosol Science and Technology, 49, 267–279, https://doi.org/10.1080/02786826.2015.1022248, 2015.

Park, K., Cao, F., Kittelson, D. B., and McMurry, P. H.: Relationship between Particle Mass and Mobility for Diesel Exhaust Particles, Environ. Sci. Technol., 37, 577–583, https://doi.org/10.1021/es025960v, 2003.

Petzold, A. and Schönlinner, M.: Multi-angle absorption photometry—a new method for the measurement of aerosol light absorption and atmospheric black carbon, Journal of Aerosol Science, 35, 421–441, https://doi.org/10.1016/j.jaerosci.2003.09.005, 2004.

Petzold, A., Schloesser, H., Sheridan, P. J., Arnott, W. P., Ogren, J. A., and Virkkula, A.: Evaluation of Multiangle Absorption Photometry for Measuring Aerosol Light Absorption, Aerosol Science and Technology, 39, 40–51, https://doi.org/10.1080/027868290901945, 2005.

Sorensen, C. M.: The Mobility of Fractal Aggregates: A Review, Aerosol Science and Technology, 45, 765–779, https://doi.org/10.1080/02786826.2011.560909, 2011.

Stephens, M., Turner, N., and Sandberg, J.: Particle identification by laser-induced incandescence in a solid-state laser cavity, Appl. Opt., 42, 3726, https://doi.org/10.1364/AO.42.003726, 2003.

Vecchi, R., Bernardoni, V., Paganelli, C., and Valli, G.: A filter-based light-absorption measurement with polar photometer: Effects of sampling artefacts from organic carbon, Journal of Aerosol Science, 70, 15–25, https://doi.org/10.1016/j.jaerosci.2013.12.012, 2014.

Yon, J., Bescond, A., and Ouf, F.-X.: A simple semi-empirical model for effective density measurements of fractal aggregates, Journal of Aerosol Science, 87, 28–37, https://doi.org/10.1016/j.jaerosci.2015.05.003, 2015.